ADVANCED FUNCTIONAL MATERIALS
www.afm-journal.de

Materials Views
www.MaterialsViews.com

Relaxor/Ferroelectric Composites: A Solution in the Quest for Practically Viable Lead-Free Incipient Piezoceramics

Claudia Groh, Daniel J. Franzbach, Wook Jo, Kyle G. Webber, Jens Kling, Ljubomira A. Schmitt, Hans-Joachim Kleebe, Soon-Jong Jeong, Jae-Shin Lee, and Jürgen Rödel*

Recently developed lead-free incipient piezoceramics are promising candidates for off-resonance actuator applications with their exceptionally large electromechanical strains. Their commercialization currently faces two major challenges: high electric field required for activating the large strains and large strain hysteresis. It is demonstrated that design of a relaxor/ferroelectric composite provides a highly effective way to resolve both challenges. Experimental results in conjunction with numerical simulations provide key parameters for the development of viable incipient piezoceramics.

1. Introduction

Over the last 20 years there has been an enormous effort in developing lead-free piezoceramics.[1–7] A new concept based on incipient piezoceramics is considered to be one of the most promising candidates for actuator applications driven at off-resonance frequencies, representatively multilayer actuators.[8] The incipient piezoceramics feature a so-called "giant" unipolar strain amounting to the bipolar strain due to the absence of remanent strain.[9,10] The use of giant strain is to distinguish the incipient piezoceramics from the conventional piezoceramics such as lead zirconate titanate (PZT) where the remanent strain due to non-180° domain switching during poling permits only half of the maximum inducible strain during unipolar loading.[11] A series of in situ diffraction studies under an electric field environment[12–15] have dictated that the structural origin of the giant strain is a reversible phase transformation between metrically cubic and non-cubic phases. The nature of each phase was identified to be, respectively, paraelectric and ferroelectric through in situ microscopy studies.[16,17] Since the discovery of the giant strain in the $(Bi_{1/2}Na_{1/2})TiO_3$-$BaTiO_3$-$(K_{0.5}Na_{0.5})NbO_3$ (BNT-BT-KNN) pseudoternary system,[10] giant strains of the same origin have been found in other BNT-based systems.[18–24]

In spite of the distinctly large strains in the incipient piezoceramics, at least two challenges have been identified for transferral into real-world applications. One is the relatively large electric field level required to trigger the giant strains and the other the large hysteresis with a strong nonlinearity.[8] A clue to resolving these challenges was given by a recent publication on a $(K_{0.5}Na_{0.5})NbO_3$-based ceramics showing more than two times larger strain than a commercial soft PZT. The origin of this exceptionally large strain behavior was attributed to its unique microstructure where each grain has a ferroelectric core and a paraelectric shell.[25] A core–shell structure was also observed in 0.91BNT-0.06BT-0.03KNN.[26] In such a core–shell structure, the ferroelectric core facilitates transition of the paraelectric shell into a ferroelectric phase by serving as a nucleus, eventually leading to a reduction in hysteretic behavior. In fact, the validity of this concept was supported by succeeding works by Lee et al.,[27,28] who demonstrated the same effect in ceramic–ceramic composites consisting of an ergodic relaxor (matrix) and a nonergodic relaxor or ferroelectric phase (seed). Here, the ergodic relaxor refers to the one that undergoes a reversible phase transition between relaxor and ferroelectric phase during electric field cycling, while the nonergodic relaxor denotes the one that transforms irreversibly into a ferroelectric phase with the application of electric field.[8] A related concept, so-called negative capacitance, has been considered in the semiconductor community as a way to enhance the capacitance of insulating gate oxide materials.[29–31]

The ceramic–ceramic composite approach to achieving desired properties dates back to 1980, when Shrout et al.[32] demonstrated that a lamellar heterogeneous material consisting of alternating layers of a ferroelectric and antiferroelectric led to a transpolarization effect. They further showed in a subsequent publication that alternating layers of ferroelectric and relaxor combined the advantages of each layer, that is, a large coupling factor (ferroelectric phase) with a good temperature stability (relaxor phase). Later, Dausch et al.[33,34] pointed out

C. Groh, Mr. D. J. Franzbach, Dr. W. Jo, Dr. K. G. Webber, Dr. J. Kling, Dr. L. A. Schmitt, Prof. H.-J. Kleebe, Prof. J. Rödel
Department of Materials and Geoscience
Technische Universität Darmstadt
Petersenstr. 23, 64287, Germany
E-mail: jo@ceramics.tu-darmstadt.de
Dr. S.-J. Jeong
Korea Electrotechnology Research Institute
Changwon, 641–120, Republic of Korea
Prof. J.-S. Lee
School of Materials Science and Engineering
University of Ulsan
Ulsan, 680–749, Republic of Korea

DOI: 10.1002/adfm.201302102

that the presence of a ferroelectric phase in an antiferroelectric matrix effectively reduced the electric field required for antiferroelectric-to-ferroelectric transition and that the changes in this field level as a function of ferroelectric phase content could be qualitatively estimated by a two-serially-connected capacitor model despite the naturally expected chemical inhomogeneity. In other functional applications, the ceramic–ceramic composite approach has been extensively utilized to tune targeted properties such as temperature stability of dielectric permittivity,[35] piezoelectric/pyroelectric properties,[36,37] reliability against cyclic loading with high electric fields,[32] dielectric tunability,[38,39] and so forth.

In this paper, we report a systematic investigation of ferroelectric/relaxor composites using 0.92BNT-0.06BT-0.02KNN as a matrix phase and 0.93BNT-0.07BT as a seed phase to demonstrate the utility of the approach in tailoring incipient piezoelectric strains. The experimental results are then compared with numerical simulation, modeling high-field ferroelectric switching and strain properties based on a series capacitor model requiring polarization coupling. From parametric studies using the model, the key material parameters that should be considered for material selection are proposed.

2. Results and Discussion

2.1. Experiment

Electric field-induced unipolar strain of composite materials at 4 kV mm^{-1} is presented in **Figure 1**a. Here, we refer to 0.93BNT-0.07BT and 0.92BNT-0.06BT-0.02KNN as seed and matrix phase, respectively. The material with 0% seed content displays a giant strain of ≈0.25% with significant hysteresis, indicating that the observed strain originates from incipient piezoelectricity.[8] The addition of 10 vol% seed material (subsequently referred to as 10% seed composition) was found to increase the maximum strain value (S_{max}) by 10%, exceeding even that of commercial soft PZT (PIC151, Lederhose, Germany). Considering the nature of induced strain in the context of incipient piezoceramics, a quantification of the degree of hysteresis is useful for a phenomenological description of the strain behavior. The level of achievable strain is closely related to the degree of instability in the field-induced ferroelectric order, that is, the less stable the induced ferroelectric order is, the larger the achievable strain becomes. Within the context of the current work, we define the degree of strain hysteresis ($\Delta S/S_{max}$) as the difference in the strain at $E_{max}/2$ normalized by S_{max}.[40] As shown in Figure 1b, the addition of seed crystals influences not only the maximum achievable strain value but also $\Delta S/S_{max}$. In the regime where the incipient piezoelectricity is active, that is, the seed content < 30%, the larger the S_{max} is, the larger the $\Delta S/S_{max}$ is. Above 30% seed content, the strain hysteresis no longer shows the incipient piezoelectric feature, corresponding to a drastic decrease in $\Delta S/S_{max}$.

The microstructure of 10% seed composition was explored over the largest possible area in the prepared sample by transmission electron microscopy. All the grains examined could be classified into two categories, grains with homogeneous and inhomogeneous contrast. **Figure 2**a provides a bright field (BF) image of a grain with a homogeneous contrast. Energy-dispersive X-ray (EDX) spectra collected from five different regions within the grain (Figure 2b) give no indication of compositional fluctuations. A distinct feature is the absence of niobium. On the other hand, a strong contrast variation was observed in the grains with an inhomogeneous contrast as exemplarily displayed in Figure 2c. These grains are featured by the presence of niobium at 16.5 and 18.6 keV (upper spectrum Figure 2d, which was collected from the grain depicted in the inset of Figure 2c). In addition, Na and K content were also found to increase in this region. It is noted that the inhomogeneous contrast does not mean that there are noticeable chemical fluctuations in the grains; in fact, all the grains were found to be chemically homogeneous regardless of the contrast variation. For comparison, a spectrum from a region showing homogeneous contrast is plotted (lower spectrum). These results

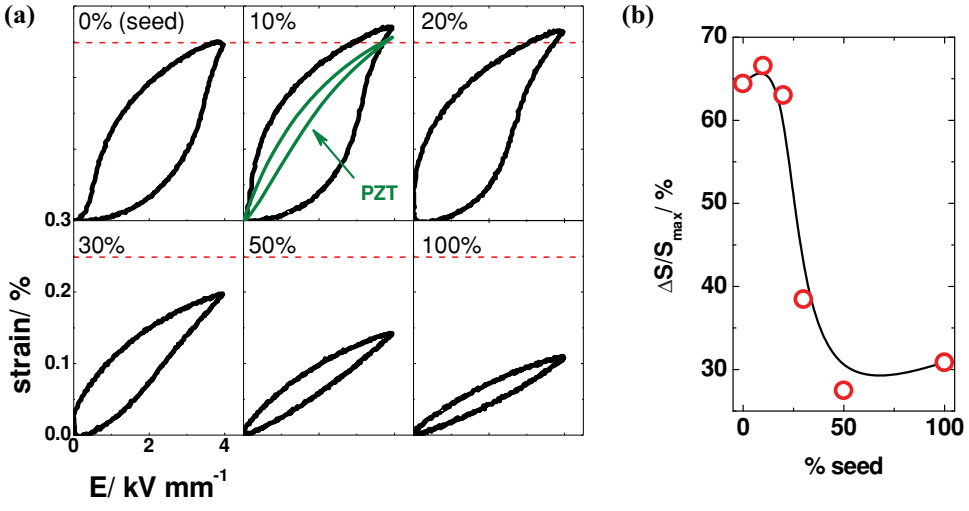

Figure 1. a) Unipolar strain hysteresis at 4 kV mm^{-1} and b) the degree of strain hysteresis defined as the difference in strain at $E_{max}/2$ as a function of seed content.

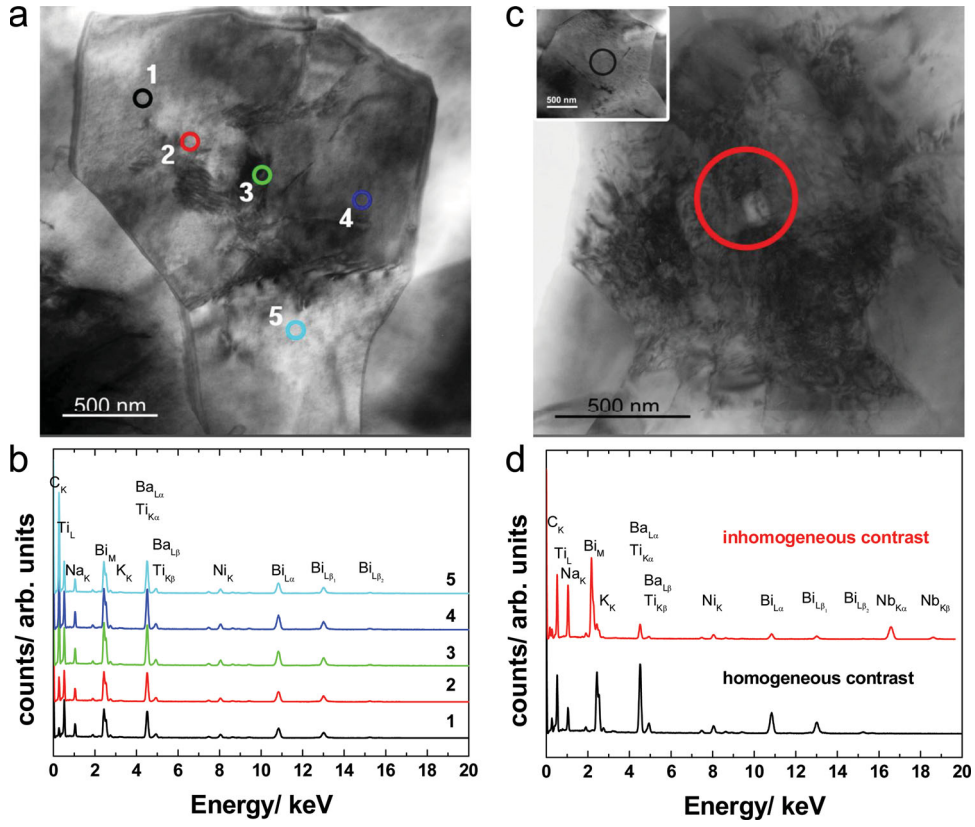

Figure 2. Bright field (BF) images of two types of grains typically encountered in 10% seed composition and related EDX spectra: a,b) homogeneous contrast in BF image and c,d) inhomogeneous contrast.

indicate that the grains showing strong contrast variation are $(K_xNa_{1-x})NbO_3$-rich phase.

The composite approach provides an additional design parameter geared towards achieving high strain at reduced electric field. Hence, the unipolar strain hysteresis curves of the matrix and the 10% seed composition are compared at 4 and 6 kV mm^{-1} (**Figure 3**a). An enhancement in the strain level due to the presence of seed crystals is evident at 4 kV mm^{-1}. At E_{max} = 6 kV mm^{-1}, however, the strain enhancement due to composite is absent. The maximum achievable strain of 10% seed composition at 4 kV mm^{-1} (≈0.38%) is slightly below that of the matrix (≈0.41%) at 6 kV mm^{-1}. Note that the achieved strain value of ≈0.38% in the 10% seed composition is approximately 90% of the induced strain in the matrix, indicating that the maximum strain achievable at saturation depends largely on the volume of matrix phase. For high electric fields (e.g., 6 kV mm^{-1} for the current compositions), the highest large-field strain coefficient, d_{33}*, is obtained for zero seed content (Figure 3b). The addition of a ferroelectric seed will slightly reduce the obtained d_{33}* but also reduce the required driving field, as demonstrated for two representative driving fields in Figure 3b.

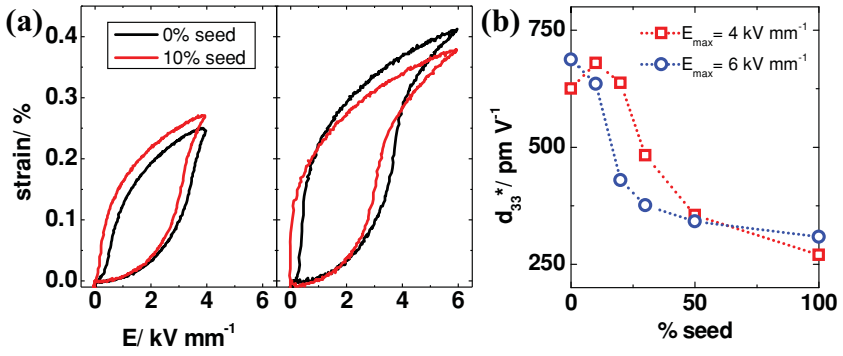

Figure 3. a) Comparison between unipolar strain hystereses of 0%- and 10%-seed compositions at two different electric field levels, namely 4 and 6 kV mm^{-1}. b) Changes in d_{33}* (i.e., S_{max}/E_{max}) as a function of seed content.

Given the fact that the giant strain originating from the incipient piezoelectricity is critically dependent upon the electric field-induced reversible phase transition from an ergodic relaxor to ferroelectric order,[8] the poling (E_{pol}) and depoling field (E_{dep}), where the field-induced ferroelectric order is established and disrupted, respectively, can be considered as critical parameters. E_{pol} and E_{dep} can be unambiguously defined at the first inflection point during electrical loading and unloading, respectively. It is important to notice here that negative E_{dep} values are possible, depending on the stability of the ferroelectric order.[41] In order for the giant unipolar strain to be fully exploited, however,

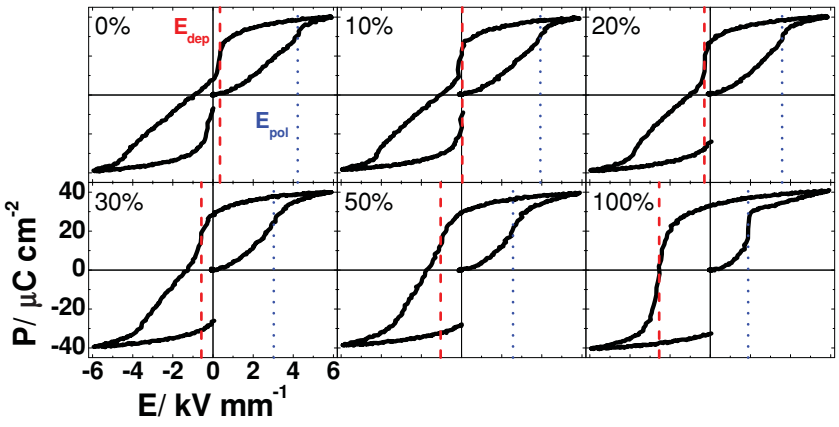

Figure 4. Polarization hysteresis curves during a bipolar poling cycle at 6 kV mm^{-1}. E_{pol} and E_{dep} are defined at the first inflection point during uphill cycle and during downhill cycle, respectively.

E_{dep} should be positive so that each unipolar cycle retraces the unipolar poling cycle.[9] Naturally, the smallest possible E_{pol} is always preferred from the practical point of view. **Figure 4** depicts the polarization hysteresis loops recorded during bipolar poling cycle at 6 kV mm^{-1}. With the addition of seed crystals, both E_{pol} and E_{dep} decrease. Note that E_{dep} coincides with the coercive field (E_c) for the 100% seed composition, indicating the absence of ergodicity that changes its phase identity during electrical cycling. Further, E_{dep} lies near 0 kV mm^{-1} in the 10% seed composition, where the maximum d_{33}* is obtained.

2.2. Modeling

We first consider an ideal capacitive composite without chemical intermixing between seed and matrix grains; thus, all the grains are joined with chemically sharp interfaces. Then, the entire system can be modeled by an equivalent circuit with two nonlinear, hysteretic capacitors connected in series. Deviation from this ideal situation could be represented by adding resistive components. In the case presented here, the magnitude of the total system polarization can be determined by Kirchhoff's voltage law. Since the polarization for each capacitor has to be the same, the externally applied voltage is distributed between both capacitors, resulting in different local electric fields on each component. The exact electric field seen by each capacitor depends on the voltage applied and the volume fraction of that component. Therefore, components with a smaller dielectric permittivity (more specifically, polarization-field gradient or large-signal permittivity) will experience a larger electric field. This implies that once an incipient piezoceramic material is mixed with a dielectric material with a larger dielectric permittivity, it is possible to induce a giant strain at electric field levels smaller than E_{pol} of the pure incipient piezoceramic.

To numerically assess the composite-induced strain enhancements, it is important to identify parameters that define the nonlinear, history-dependent polarization hysteresis. Considering the fact that the composite effect depends not only on the seed content but also on E_{max} during cycling, the shape-determining parameters can be grouped into two categories: one is E_{max}-dependent and the other not. **Figure 5** presents a part of the polarization hysteresis during a bipolar poling cycle at different levels of E_{max}. Two features are noted: i) both E_{pol} and E_{dep} show little change regardless of the magnitude of E_{max} and ii) both P_{rem} and P_{max} change significantly with the magnitude of E_{max}.

To effectively trace the change in the key shape determining parameters as a function of seed content, $P(E)$ loops for the seed and matrix compositions are divided into eight segments with various tangent lines drawn at the points of physical significance, as illustrated in **Figure 6**. Segment 1 represents an electrostrictive regime, where field-induced changes take place reversibly. Segment 2 is a transition regime, where either a long-range ferroelectric order develops in the case of relaxor ferroelectrics or the majority of domains switch in the case of normal ferroelectrics. In this regime, experimental observation dictates that polarization decay is given by a weighted average between segments 1 and 4 for the case where E_{max} lies in this region. Segment 3 is a saturation regime, where the polarization value linearly increases with increasing electric field. In the case of the matrix composition (Figure 6b), an additional line is inserted between 1 and 2 to better describe the actual $P(E)$ loop. This is necessary because the transition regime is too large to be described by a single segment. As well, a different path, that is, 1u-2u'-2u in Figure 6b, is taken in describing the unipolar cycle of the matrix composition after the poling treatment due to a remanent state after poling.

Using the segmented $P(E)$ curves as input data, $P(E)$ loops of selected compositions are simulated by resolving the voltage distribution between each nonlinear, hysteretic capacitor with a binary minimization algorithm. During simulation the loading/unloading path was divided into smaller segments. The equivalent circuit model is compared to experimentally obtained data in **Figure 7**. The seed concentration was varied by increasing the simulated thickness, that is, volume fraction, of the capacitor that represents the seed phase. The model is in good agreement with experimental measurements in terms of

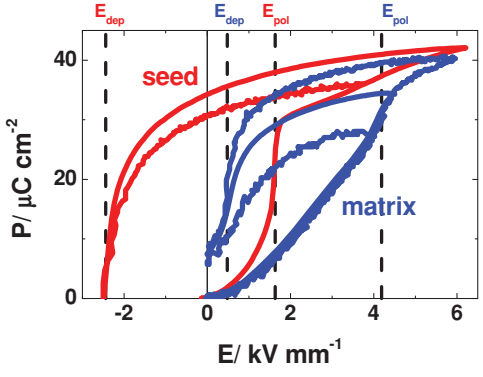

Figure 5. Electric-field-dependent (P_{rem}, P_{max}) and -independent (E_{pol}, E_{dep}) parameters.

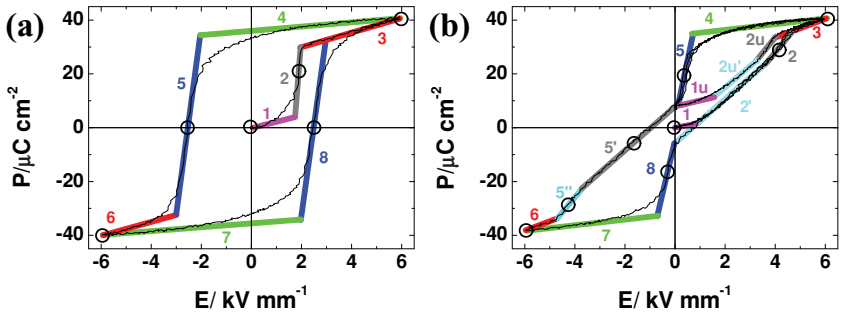

Figure 6. *P*(*E*) loop of a) the seed and b) the matrix, segmented with the tangent lines drawn at each points of significance.

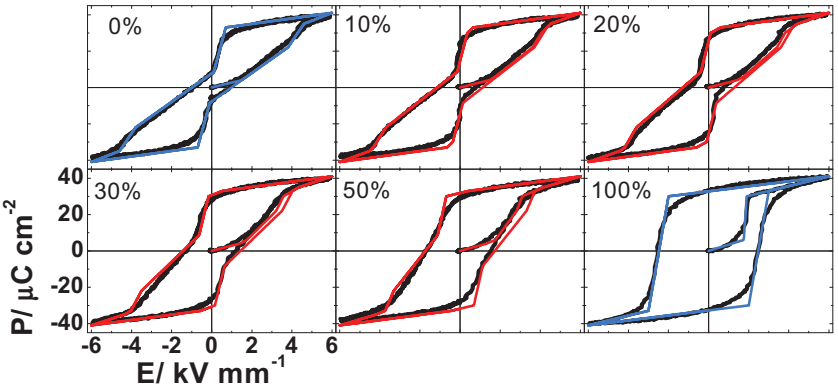

Figure 7. Simulated and experimental polarization hysteresis curves during a bipolar poling cycle at 6 kV mm^{-1}.

the hysteresis loop evolution as a function of seed concentration. E_{pol} and E_{dep}, which play an important role in realizing practically viable giant strains, have been determined from the simulations and are compared to experimental data as a function of seed content (**Figure 8**). E_{pol} is seen to drastically decrease up to ≈40% seed content, which coincides with the point where the enhancement in d_{33}* due to incipient piezoelectricity becomes insignificant (cf., Figure 1a). Above 40% seed content, E_{pol} was found to decrease linearly with increasing seed content. On the other hand, E_{dep} decreases monotonically throughout the compositional range except for the 100%-seed composition. The sudden change in E_{dep} at 100% seed composition implies that as long as any amount of the matrix phase remains in the system, the polarization-electric field behavior is affected by the depolarization field imposed by the matrix phase during bipolar cycling. This can also be observed by the presence of a trace of constriction in *P*(*E*) hysteresis loop.

To estimate d_{33}*, strain hysteresis loops, *S*(*E*), corresponding to each *P*(*E*) simulated by the equivalent circuit model are constructed using a phenomenological equation, $S = Q_{11}P^2$, where Q_{11} denotes the electrostrictive coefficient.[8] The effective Q_{11} for each composition is approximated by a linear rule of mixtures between the values fitted to the seed (0.0265 m^4 C^{-2}) and matrix phases (0.0240 m^4 C^{-2}). **Figure 9** depicts the simulated d_{33}* for various E_{max} values as a function of seed content using Q_{11} estimated from 6 kV mm^{-1} strain data. The d_{33}* values presented here were all determined from the second cycle of two successive unipolar cycles. A comparison with the experimental data reveals that the model is accurately able to predict the observed composition dependent trend at both 4 and 6 kV mm^{-1}, though the absolute values at 4 kV mm^{-1} deviate from the experimental values. This deviation in the absolute value was found to originate from the use of Q_{11} derived at 6 kV mm^{-1} data; the deviation of the currently investigated strain data from electrostriction causes Q_{11} to depend on E_{max}. For example, the use of Q_{11} from 4 kV mm^{-1} results in good agreement between the experimental and calculated values for 4 kV mm^{-1} (Figure S1, Supporting Information).

At 1 kV mm^{-1} in the electrostrictive regime for both the seed and matrix phase, d_{33}* is the highest at 100% seed composition due to its larger electrostrictive coefficient in comparison to the matrix. With increasing seed content, d_{33}* is predicted to monotonically decrease. When E_{max} = 2 kV mm^{-1}, which is

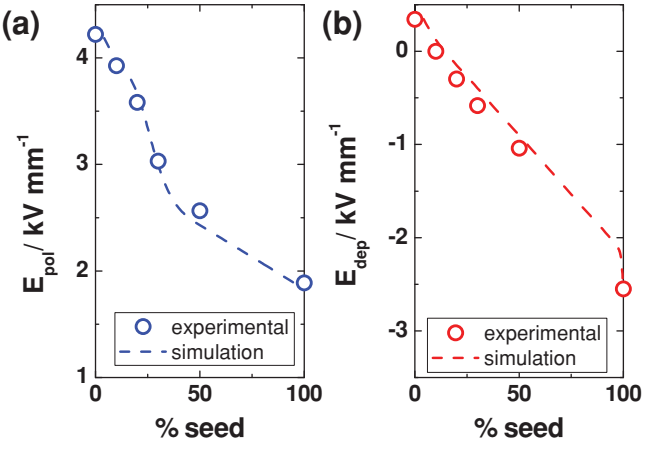

Figure 8. a) E_{pol} and b) E_{dep} as a function of seed content from experimental data and simulations.

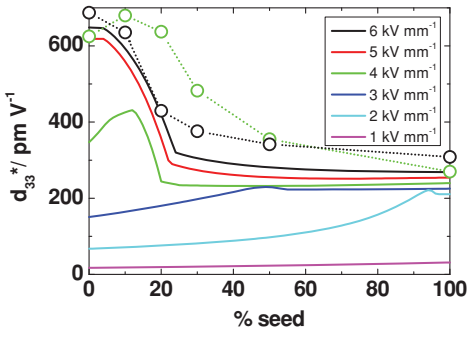

Figure 9. Simulated d_{33}* as a function of seed content at various E_{max} in comparison with experimental data.

large enough to bring the seed phase into a saturated regime, a composite-induced strain enhancement starts to appear. This is manifested as a peak in d_{33}* in the seed-rich compositions. It signifies a composite-induced strain enhancement and shifts towards the matrix-rich compositions with increasing E_{max} up to 4 kV mm^{-1}, above which the peak consistently stays at 0% seed composition with the composite approach no longer effective in enhancing d_{33}*.

The peak position shift can be understood in terms of variations in the electric field distribution between matrix and seed phases. Due to differences in field-dependent polarization and changes in volume content, the increasing seed material content decreases the electric field in the matrix phase. As long as the field level does not suffice for inducing incipient piezoelectric strain in the matrix phase, more seed phase is required to achieve a larger S_{max}. On the other hand, when the field level is large enough to activate incipient piezoelectric strain in the matrix phase, the electric field distribution at 0 kV mm^{-1} plays a critical role in the maximum achievable d_{33}* through the magnitude of remanent strain. The coexistence of seed and matrix phases with different capacitances prompts a remanent electric field in both the seed and matrix. For a giant strain to be realized, the remanent electric field of the matrix phase should be smaller than E_{dep}, which requires a negative field on the seed phase. Given the fact that the polarization level of the matrix increases with electric fields larger than E_{pol} (Figure 5), the seed volume fraction is required to remain smaller to effectively reduce the remanent electric field in the matrix phase. The smaller the seed volume fraction, the larger the magnitude of remanent electric field in the seed phase, which is negative in sign. Therefore, the peak in d_{33}* in the d_{33}*-composition space shifts towards the matrix-rich side. Here, the imposed negative field causes a reduction in S_{rem} and consequently enhances d_{33}*.

Figure 10 shows the dependence of d_{33}* at 4 kV mm^{-1} on two key parameters that can be used for material selection. For reference, the d_{33}* for the pure matrix phase (horizontal lines) and the values from the composite material used in this study (vertical lines) are represented as dashed lines. An illustration for the calculation scheme is provided in Figure S2 (Supporting Information). The composite effect is maximized under two conditions: a) the seed phase is chosen in a way that the remanent polarization of the seed phase is comparable to the saturated polarization of the matrix phase and b) the coercive field of the seed phase is lower than the poling field of the matrix phase. Generally speaking, it is important for the seed phase to have a large remanent polarization relative to the matrix to facilitate the shifting of field onto the matrix, allowing the field induced phase transition to occur at lower electric fields. Importantly, E_{dep} for the composite material remains positive in this region. Interestingly, however, there is an apparent theoretical maximum in achievable d_{33}* through the adjustment of the remanent and saturation polarizations of the seed and matrix end members, which is found at approximately $P_r^{seed}/P_s^{matrix} = 1$. This is because polarization saturation in the ferroelectric material (segment 3, Figure 6a) is never reached during electrical loading when the remanent polarization is too large relative to the matrix material.

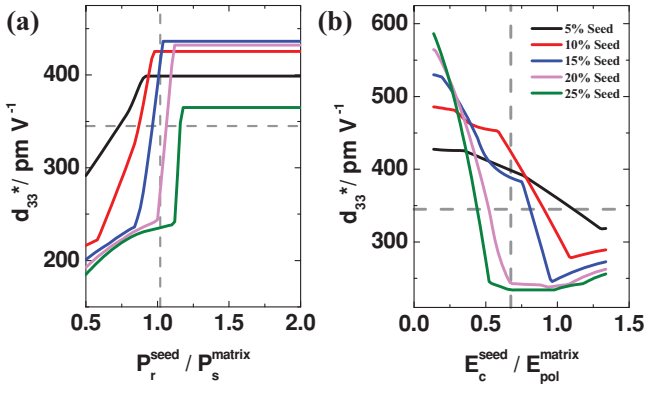

Figure 10. Parametric study of d_{33}* as a function of a) P_r^{seed}/P_s^{matrix} and b) $E_c^{seed}/E_{pol}^{matrix}$ for different seed contents at 4 kV mm^{-1}.

It is also possible to change the observed d_{33}* through adjusting the coercive field of the seed relative to the poling field of the matrix, while holding the remanent and saturation polarizations constant. A reduction in $E_c^{seed}/E_{pol}^{matrix}$ leads to an enhancement of d_{33}* for all compositions, resulting in an earlier transferral of electric field from the seed to the matrix, decreasing the electric field required for generating incipient piezoelectricity. Additionally, at lower coercive field values, it is possible for the ferroelectric seed material to lose the electric field induced polarization due to the requirement that both components, that is, seed and matrix, always retain the same polarization (not the same field). In the remanent state this results in the ferroelectric material having a negative electric field, which may be large enough to cause reverse switching, and the matrix material in having a positive electric field. This polarization switching in the seed was found to enhance the d_{33}*. Interestingly, the model predicts a further slight enhancement in d_{33}* with increasing $E_c^{seed}/E_{pol}^{matrix}$ values above approximately 1. In this regime the applied electric field is no longer large enough to reach the saturation regime of the seed material (segment 3, Figure 6a). During unloading the seed follows a path with a slope defined as a linear combination of the slopes in segments 1 and 4, which linearly depends on the maximum polarization reached. With an increasing coercive field there is a decrease in the maximum and remanent seed polarization reached, resulting in an increase of the slope during unloading. The change in slope is found to slightly enhance the d_{33}* at larger values of $E_c^{seed}/E_{pol}^{matrix}$. This effect will saturate at even higher $E_c^{seed}/E_{pol}^{matrix}$ values, where the electric field on the seed is no longer large enough to reach segment 2 (Figure 6a).

4. Conclusions

The ferroelectric/relaxor composite approach was studied on a model system using nonergodic relaxor 0.93BNT-0.07BT and ergodic relaxor 0.92BNT-0.06BT-0.02KNN, aiming for tailoring strain properties of incipient piezoceramics. Featured advantages of this approach were identified as a reduction in the critical electric field required for triggering giant strain as well as in strain hysteresis. Two different types of grains, chemically distinctive in terms of Nb content, were observed by transmission electron microscopy. A simple numerical model based on the rule of mixture between two serially-connected capacitors

successfully rationalized the experimental observations. Three key variables were proposed for optimizing the strain properties of composites such as maximum driving field (E_{max}), ratio between P_r^{seed} and P_s^{matrix}, and the ratio between E_c^{seed} and E_{pol}^{matrix}.

5. Experimental Section

Materials: The calcined seed, $0.93(Bi_{1/2}Na_{1/2}TiO_3)$-$0.07(BaTiO_3)$, and matrix, $0.92(Bi_{1/2}Na_{1/2}TiO_3)$-$0.06(BaTiO_3)$-$0.02(K_{0.5}Na_{0.5}NbO_3)$, powders were prepared by a standard mixed oxide route. The oxide or carbonates of the respective elements, namely, Bi_2O_3 (99.975% purity), $BaCO_3$ (99.8% purity), K_2CO_3 (99.0% purity), $NaCO_3$ (99.5% purity), TiO_2 (99.6% purity), and Nb_2O_5 (99.9% purity) (all Alfa Aesar GmbH & Co. KG, Karlsruhe, Germany), were mixed according to their stoichiometric formula and ball-milled in ethanol for 24 h. The dried slurries were calcined for 2 h at 700 °C, followed by 3 h at 800 °C. The seed powder was ball-milled for 20 min, while the matrix was ball-milled for 24 h. To form composite samples, dried seed and matrix powders were mixed in different vol% ratios, namely 0:100, 10:90, 20:80, 30:70, 50:50, 100:0, respectively, and mixed for 30 min on a rolling bank. The composite powders were uniaxially pressed into pellets of 10 mm in diameter and further compacted by cold isostatic pressing at 300 MPa. Sintering was carried out at 1100 °C for 3 h in covered alumina crucibles. To minimize the evaporation of volatile elements during sintering, the pellets were covered in atmospheric powder of the respective compositions. The pellets were ground down to approximately 650 µm and painted with silver paste which was burnt in at 450 °C to form the electrodes.

Methods: The polarization and strain hysteresis were measured by means of a Sawyer-Tower setup with an optical sensor (Philtec, Inc., Annapolis, Maryland) at a frequency of 50 mHz. Maximum electric fields of 4 and 6 kV mm^{-1} were applied. Samples for transmission electron microscopy (TEM) were prepared by a standard procedure of polishing, ultrasonic disc cutting, dimpling, and Ar^+ ion milling. Specimens were slightly coated with carbon in order to avoid charging under the electron beam. Experiments were performed on an FEI CM20 microscope operated at 200 kV. EDX spectra were obtained with an Oxford TEM 250 Silicon Drift Detector.

Supporting Information

Supporting Information is available from the Wiley Online Library or from the author.

Acknowledgements

This work was financially supported by the Deutsche Forschungsgemeinschaft (DFG) under SFB595. C.G. acknowledges financial support from the state center AdRIA on adaptronics. J.S.L. thanks the National Research Foundation of Korea (NRF) under Grant number 2012K1A2B1A03000668 for financial support.

Received: June 20, 2013
Revised: July 26, 2013
Published online: September 6, 2013

[1] L. E. Cross, *Nature* **2004**, *432*, 24.
[2] K. Wang, F. Yao, W. Jo, D. Gobeljic, V. V. Shvartsman, D. C. Lupascu, J.-F. Li, J. Rödel, *Adv. Funct. Mater.* doi: 10.1002/adfm.201203754.
[3] W. Liu, X. Ren, *Phys. Rev. Lett.* **2009**, *103*, 257602.
[4] T. Takenaka, H. Nagata, Y. Hiruma, *Jpn. J. Appl. Phys.* **2008**, *47*, 3787.
[5] J. Rödel, W. Jo, K. T. P. Seifert, E.-M. Anton, T. Granzow, D. Damjanovic, *J. Am. Ceram. Soc.* **2009**, *92*, 1153.
[6] T. R. Shrout, S. J. Zhang, *J. Electroceram.* **2007**, *19*, 113.
[7] D. Damjanovic, N. Klein, J. Li, V. Porokhonskyy, *Funct. Mater. Lett.* **2010**, *3*, 5.
[8] W. Jo, R. Dittmer, M. Acosta, J. Zang, C. Groh, E. Sapper, K. Wang, J. Rödel, *J. Electroceram.* **2012**, *29*, 71.
[9] W. Jo, T. Granzow, E. Aulbach, J. Rödel, D. Damjanovic, *J. Appl. Phys.* **2009**, *105*, 094102.
[10] S.-T. Zhang, A. B. Kounga, E. Aulbach, H. Ehrenberg, J. Rödel, *Appl. Phys. Lett.* **2007**, *91*, 112906.
[11] H. Kungl, M. J. Hoffmann, *Acta Mater.* **2007**, *55*, 5780.
[12] J. E. Daniels, W. Jo, J. Rödel, V. Honkimäki, J. L. Jones, *Acta Mater.* **2010**, *58*, 2103.
[13] M. Hinterstein, M. Knapp, M. Hölzel, W. Jo, A. Cervellino, H. Ehrenberg, H. Fuess, *J. Appl. Cryst.* **2010**, *43*, 1314.
[14] A. J. Royles, A. J. Bell, A. P. Jephcoat, A. K. Kleppe, S. J. Milne, T. P. Comyn, *Appl. Phys. Lett.* **2010**, *97*, 132909.
[15] W. Ge, Q. Zhang, Z. Wang, J. Yao, J. Li, H. Luo, D. Viehland, *Phys. Status Solidi RRL* **2011**, *5*, 356.
[16] R. Dittmer, W. Jo, J. Rödel, S. Kalinin, N. Balke, *Adv. Funct. Mater.* **2012**, *22*, 4208.
[17] J. Kling, X. Tan, W. Jo, H.-J. Kleebe, H. Fuess, J. Rödel, *J. Am. Ceram. Soc.* **2010**, *93*, 2452.
[18] Y. Hiruma, Y. Imai, Y. Watanabe, H. Nagata, T. Takenaka, *Appl. Phys. Lett.* **2008**, *92*, 262904.
[19] R. Dittmer, W. Jo, J. Daniels, S. Schaab, J. Rödel, *J. Am. Ceram. Soc.* **2011**, *94*, 4283.
[20] H.-S. Han, W. Jo, J.-K. Kang, C.-W. Ahn, I. Won Kim, K.-K. Ahn, J.-S. Lee, *J. Appl. Phys.* **2013**, *113*, 154102.
[21] A. Hussain, C. W. Ahn, J. S. Lee, A. Ullah, I. W. Kim, *Sens. Actuators A* **2010**, *158*, 84.
[22] K.-N. Pham, A. Hussain, C. W. Ahn, W. Kim, S. J. Jeong, J.-S. Lee, *Mater. Lett.* **2010**, *64*, 2219.
[23] E. A. Patterson, D. P. Cann, J. Pokorny, I. M. Reaney, *J. Appl. Phys.* **2012**, *111*, 094105.
[24] J. Hao, B. Shen, J. Zhai, C. Liu, X. Li, X. Gao, *J. Appl. Phys.* **2013**, *113*, 114106.
[25] S.-Y. Choi, S.-J. Jeong, D.-S. Lee, M.-S. Kim, J.-S. Lee, J. H. Cho, B. I. Kim, Y. Ikuhara, *Chem. Mater.* **2012**, *24*, 3363.
[26] L. A. Schmitt, H.-J. Kleebe, *Funct. Mater. Lett.* **2010**, *03*, 55.
[27] D. S. Lee, D. H. Lim, M. S. Kim, K. H. Kim, S. J. Jeong, *Appl. Phys. Lett.* **2011**, *99*, 062906.
[28] D.-S. Lee, S.-J. Jeong, E.-C. Park, J.-S. Song, *J. Electroceram.* **2006**, *17*, 505.
[29] A. Q. Jiang, H. J. Lee, G. H. Kim, C. S. Hwang, *Adv. Mater.* **2009**, *21*, 2870.
[30] S. Salahuddin, S. Datta, *Nano Lett.* **2008**, *8*, 405.
[31] T. N. Theis, P. M. Solomon, *Science* **2010**, *327*, 1600.
[32] T. R. Shrout, W. A. Schulze, J. V. Biggers, *Ferroelectrics* **1980**, *29*, 129.
[33] D. E. Dausch, E. Furman, F. Wang, G. H. Haertling, *Ferroelectrics* **1996**, *177*, 221.
[34] D. E. Dausch, E. Furman, F. Wang, G. H. Haertling, *Ferroelectrics* **1996**, *177*, 237.
[35] O. Furukawa, M. Harata, M. Imai, Y. Yamashita, S. Mukaeda, *J. Mater. Sci.* **1991**, *26*, 5838.
[36] H. Komiya, Y. Naito, T. Takenaka, K. Sakata, *Jpn. J. Appl. Phys., Part 1* **1989**, *28*, 114.
[37] A. Yoneda, T. Takenaka, K. Sakata, *Jpn. J. Appl. Phys., Part 1* **1989**, *28*, 95.
[38] V. O. Sherman, A. K. Tagantsev, N. Setter, *Appl. Phys. Lett.* **2007**, *90*, 162901.
[39] V. O. Sherman, A. K. Tagantsev, N. Setter, D. Iddles, T. Price, *J. Appl. Phys.* **2006**, *99*, 074104.
[40] Piezoelectric actuators and ultrasonic motors, (Ed: K. Uchino), Kluwer Academic Publishers, Boston **1997**.
[41] W. Jo, E. Erdem, R.-A. Eichel, J. Glaum, T. Granzow, D. Damjanovic, J. Rödel, *J. Appl. Phys.* **2010**, *108*, 014110.